

Perspectives of running self-consistent DMFT calculations for strongly correlated electron systems on noisy quantum computing hardware

Jannis Ehrlich,¹ Daniel F. Urban,^{1,2} and Christian Elsässer^{1,2}

¹*Fraunhofer-Institut für Werkstoffmechanik IWM, Wöhlerstraße 11, Freiburg, Germany*

²*Freiburger Materialforschungszentrum, Universität Freiburg, Stefan-Meier-Straße 21, Freiburg, Germany*

Dynamical Mean Field Theory (DMFT) is one of the powerful computational approaches to study electron correlation effects in solid-state materials and molecules. Its practical applicability is, however, limited by the exponential growth of the many-particle Hilbert space with the number of considered electronic orbitals. Here, the possibility of a one-to-one mapping between electronic orbitals and the state of a qubit register suggests a significant computational advantage for the use of a Quantum Computer (QC) for solving DMFT models. In this work we present a QC approach to solve a two-site DMFT model based on the Variational Quantum Eigensolver (VQE) algorithm. We discuss the challenges arising from stochastic errors and suggest a means to overcome unphysical features in the self-energy. We thereby demonstrate the feasibility to obtain self-consistent results of the two-site DMFT model based on VQE simulations with a finite number of shots. We systematically compare results obtained on simulators with calculations on the IBMQ Ehningen QC hardware.

I. INTRODUCTION

The understanding and design of functional materials and molecules is nowadays widely supported by computational studies. On the atomic scale, density functional theory (DFT) is the widely used tool to calculate various physical properties for a large class of materials at reasonable accuracy and numerical cost [1]. However, DFT cannot correctly capture the physics of strongly correlated electron systems. This shortcoming originates from the exchange-correlation functional, for which only approximate forms are available, such that the interactions between electrons are only treated on a mean field level.

One approach to overcome these limitations is the dynamical mean field theory (DMFT) [2, 3]. It exploits that electronic interactions are strongest on short distances as for example in the partially filled *d*-shells of transition metal atoms or *f*-shells of rare earth atoms. DMFT is based on the equivalence of two notions of a correlated orbital: (i) as an impurity connected to an uncorrelated bath in terms of an Anderson impurity model (AIM) [4] and (ii) as part of a regular crystal lattice. These two notions lead to a self-consistency condition formulated in terms of Green's functions (GF).

In practice, DMFT calculations are routinely performed for real materials with finite system sizes [5–12] and provide a good insight into the physics of strong electron correlations. The bottleneck in these calculations is the solution of the AIM because the corresponding Hamiltonian matrix scales exponentially in the number of orbitals. This limits a solution via exact diagonalization (ED) in general to ~ 24 orbitals [13], while some modifications even allow up to ~ 100 orbitals [14]. Quantum Monte Carlo (QMC) methods on the other hand are limited by their fermion sign problem [15]. Further approaches exist to solve the AIM, e.g. the numerical renormalization group [16] method, which come with their own limitations.

In addition to the above mentioned approaches which are applicable on classical computers, first hybrid classical-quantum computing algorithms were presented recently which have the potential to solve the AIM [17–22]. In the spirit of Feynman's idea [23], these algorithms use quantum computers to simulate equivalent quantum systems. In these approaches, each fermionic spin-orbital of the original system is mapped to one qubit, such that the exponential scale of the Hilbert-space becomes a linear scale in the number of qubits. Current QC devices already have several hundred qubits, and thus in principle they allow the simulation of a few hundred orbitals, going far beyond the capability of any classical computer. However, even the lowest noise rates that were achieved on a real device so far are still too large for reliable calculations, such that only small systems can be simulated reasonably well.

The hybrid approaches to obtain the GF as a solution of a model Hamiltonian like the AIM mainly belong to three different types: Time evolution approaches [17–20, 22, 24, 25], Lehmann representation approach [21, 22] and subspace-matrix approaches [26–28]. The minimal realization of a DMFT approach is the two-site DMFT model which was introduced in Ref. [29]. This model was already considered as a test case for hybrid classical-quantum computer algorithms, namely the time-evolution approaches in Refs. [18–20, 25] and the Lehmann representation approach in Ref. [21]. In the case of time-evolution, the required long circuits include high two-qubit gate counts and lead to a significant noise rate on current hardware. Thus, in [18–20] the Fourier transform from time to frequency domain is performed by fitting Fourier coefficients of the analytically known frequency representation to the GF in time domain. Steckmann et al. [25] overcame this limitation, but still exploit the particle-hole symmetry for determining the quasi-particle weight used for the DMFT convergence. Therefore, this approach cannot easily be generalized to more complex models of more than two sites.

In this work we investigate the challenges that arise for the Lehmann-based hybrid classical-quantum approach to DMFT on Noisy Intermediate-Scale Quantum (NISQ) computer systems by studying the two-site DMFT model [29] as an example. The paper is organized as follows. We first introduce the general DMFT approach, as well as the two-site DMFT specifics in Sec. II. In Sec. III we then discuss the mapping of the AIM to a quantum computer and our approach to obtain its full GF. Section IV presents the different noise models and the error mitigation strategy used in our study. In Sec. V we discuss the results for the different steps of the quantum algorithm with increasing complexity in the QC contribution, including calculations on cloud quantum computers. First, we investigate only the eigenvalues and eigenstates (Sec. VA), then we construct the GF and the self-energy (Sec. VB). Since unphysical features appear in the self-energy, we introduce an efficient fitting procedure to avoid artifacts arising from the use of approximate results. We then first approximate the required quantum resources for a full self-consistent DMFT simulation (Sec. VC), then perform this simulation (Sec. VD), and apply the developed work flow to investigate the Mott-insulator transition of the two-site DMFT model (Sec. VE). Throughout our analysis we verify the correctness of the hybrid algorithm by an ideal noiseless simulation based on linear algebra. In a second step, we account for the probabilistic nature of quantum mechanics which manifests itself in the measurement process on the quantum computer and study the effect of shot noise on the performance of the algorithm. The influences of gate, readout and decoherence errors are subsequently studied using a simulator with tunable error rates. Our analysis is complemented by results obtained on the IBMQ System One Ehning, a superconducting 27-qubit Falcon r5.11 processor.

II. DYNAMICAL MEAN FIELD THEORY

The Hubbard model provides the simplest model for the description of a correlated electron system [30]. Its Hamiltonian

$$H_{\text{Hub}} = -t \sum_{\langle i,j \rangle, \sigma} c_{i,\sigma}^\dagger c_{j,\sigma} + U \sum_i n_{i,\uparrow} n_{i,\downarrow} \quad (1)$$

includes the movement (hopping) of electrons between neighboring lattice sites i and j with hopping energy t and the interaction between electrons with strength U , which acts only between two electrons with opposite spin when they occupy the same lattice site. Here $c_{i,\sigma}^\dagger$ and $c_{i,\sigma}$ are the creation and annihilation operators of an electron with spin σ at site i , respectively, and $n_{i,\sigma} = c_{i,\sigma}^\dagger c_{i,\sigma}$ is the particle number operator on site i . In spite of its seeming simplicity, this model is not analytically solvable in more than one spatial dimension.

The DMFT divides the solution of the Hubbard model into two tasks: First, the full lattice is described by GF

G_{lat} which requires self-energies Σ which are assumed to be local. Second, the self-energy can be efficiently calculated by an auxiliary model consisting of a single site with interacting orbitals which is coupled to an effective bath. This bath has to be parametrized in such a way, that it represents the crystal lattice surrounding the specific site. Coupling the two tasks has the additional challenge, that the solution has to be determined self-consistently. (For reviews on DMFT see e.g. Ref. [5, 8].) The auxiliary model system is the AIM with the Hamiltonian

$$H_{\text{AIM}} = H_{\text{imp}} + H_{\text{bath}} + H_{\text{hyb}} \quad (2)$$

$$H_{\text{imp}} = \varepsilon_d \sum_{\sigma} d_{\sigma}^\dagger d_{\sigma} + U d_{\uparrow}^\dagger d_{\uparrow} d_{\downarrow}^\dagger d_{\downarrow} \quad (3)$$

$$H_{\text{bath}} = \sum_{k,\sigma} \varepsilon_k c_{k,\sigma}^\dagger c_{k,\sigma} \quad (4)$$

$$H_{\text{hyb}} = \sum_{k,\sigma} V_k (d_{\sigma}^\dagger c_{k,\sigma} + c_{\sigma}^\dagger d_{k,\sigma}). \quad (5)$$

The AIM describes a single impurity site $d_{\sigma}^\dagger |0\rangle$ with single-particle energy ε_d where electrons of opposite spin interact with strength U . This impurity is connected to a bath of non-interacting sites $c_{k,\sigma}^\dagger |0\rangle$ with energy ε_k via a hybridization strength V_k .

The central quantity in DMFT is the GF which has to be determined self-consistently. Based on the equivalence of the two models, the lattice GF on the impurity site G_{lat} has to be identical to the impurity GF G_{imp} in the AIM. This directly implies the equivalence of the self-energy of both systems. In the limit of infinitely many bath sites this DMFT approach becomes exact [2].

The simplest possible DMFT model consists of only one impurity and one bath site, $H_{\text{bath}} = \sum_{\sigma} \varepsilon_c c_{\sigma}^\dagger c_{\sigma}$. This so-called two-site DMFT, which we consider in this paper, was studied in detail by Potthoff [29]. He derived two specific conditions for self-consistency,

$$n_{\text{imp}} = n \quad \text{and} \quad V^2 = z M_2^{(0)}. \quad (6)$$

These conditions demand that the occupation of the correlated site has to be equal in both formulations of the problem and the hybridization strength V must be equal to the product of the quasi-particle weight z and the variance of the non-interacting density of states, i.e. the bandwidth of the bath electrons, $M_2^{(0)} = \sum_{i \neq j} t_{ij}^2 = \int d\omega \omega^2 \rho_0(\omega)$.

In our practical calculation we proceed according to the following protocol:

- (0) Start with an initial guess for the bath energies ε_c and the hybridization strength V .
- (1) Solve the AIM with parameters ε_c and V under the constraint $V^2 = z M_2^{(0)}$.
- (2) Calculate the occupation of the impurity given by $n_{\text{imp}} = \frac{2}{\pi} \int_{-\infty}^0 d\omega \text{Im} G_{\text{imp}}(\omega + i0^+)$, where 0^+ refers to an infinitesimal shift to the positive half plane.

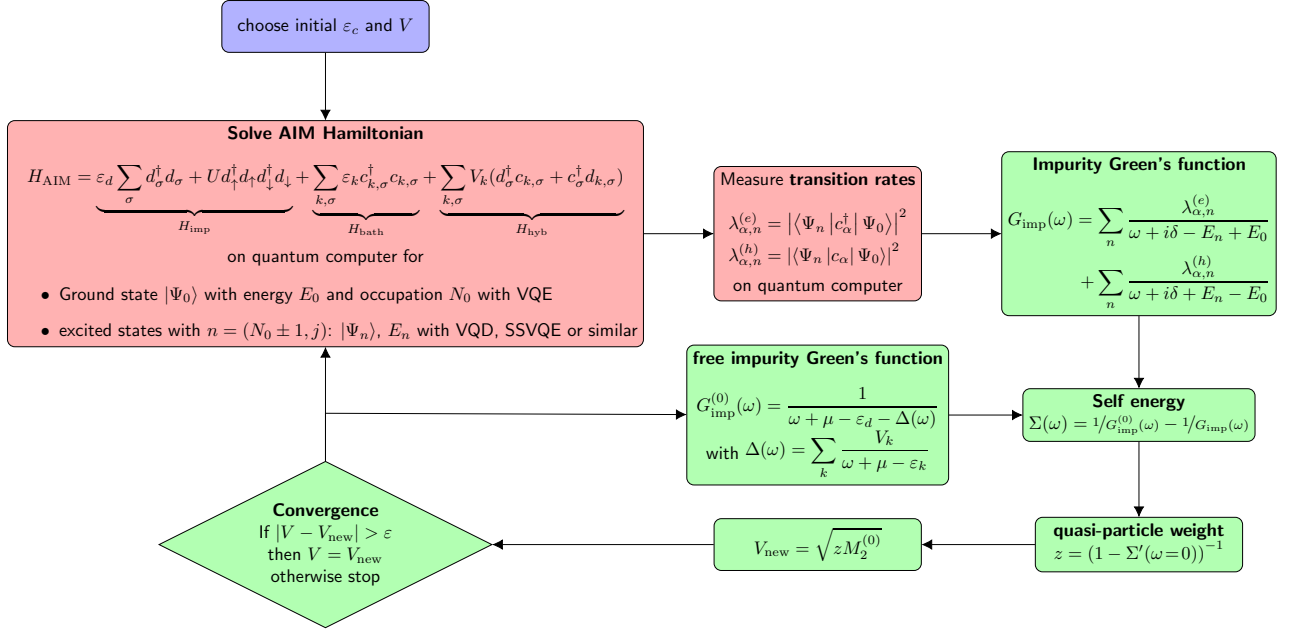


FIG. 1. Schematic illustration of the inner self-consistency loop for the two-site DMFT model for determining the hybridization strength V while keeping the impurity occupation n_{imp} constant. Red boxes indicate operations performed on a quantum computer while green boxes indicate purely classical computations.

- (3) Calculate the band-filling (cf. Ref. [29], Eq. (25)) via $n = 2 \int_{-\infty}^0 d\omega \rho_0[\omega + \mu - \Sigma(\omega)]$,
- (4) Determine a new ε_c (using a classical optimizer) that reduces $\delta n = |n_{\text{imp}} - n|$ and restart from step 1 until δn is sufficiently small.

Besides the outer self-consistency loop (1)–(4) for the occupation number, an inner self-consistency cycle is needed in step (1) in order to ensure Potthoff's second condition $V^2 = zM_2^{(0)}$. Here, the protocol which is illustrated schematically in Fig. 1 consists of the following steps (for a detailed discussion including the equations see Refs. [29] and [21])

- (1.1) Solve the AIM (Eq. (2)) for the chosen parameters ε_c and V and obtain eigenenergies E_i and eigenstates $|\Psi_i\rangle$ of H_{AIM} .
- (1.2) Calculate the impurity GF based on the Lehmann representation

$$G_{\text{imp}}(\omega) = \sum_n \frac{|\langle \Psi_n | c_{\alpha}^{\dagger} | \Psi_0 \rangle|^2}{\omega + i\delta - E_n + E_0} + \sum_n \frac{|\langle \Psi_n | c_{\alpha} | \Psi_0 \rangle|^2}{\omega + i\delta + E_n - E_0} \quad (7)$$

- (1.3) Calculate the free impurity GF by

$$G_{\text{imp}}^{(0)}(\omega) = \frac{1}{\omega + \mu - \varepsilon_d - \Delta(\omega)} \quad (8)$$

with hybridization function $\Delta(\omega) = \sum_k \frac{V_k}{\omega + \mu - \varepsilon_k}$

- (1.4) Calculate the self-energy by the inverted Dyson equation

$$\Sigma(\omega) = [G_{\text{imp}}^{(0)}(\omega)]^{-1} - [G_{\text{imp}}(\omega)]^{-1} \quad (9)$$

- (1.5) Obtain the quasi-particle weight

$$z = \left(1 - \frac{d\Sigma(\omega)}{d\omega} \Big|_{\omega=0} \right)^{-1} \quad (10)$$

- (1.6) Update the hybridization strength $V = \sqrt{zM_2^{(0)}}$

- (1.7) Start from step 1.1 until a self-consistent V is obtained

In practice, it is convenient to stabilize the convergence by using an appropriate mixing when updating the hybridization strength in step (1.6) before starting the next iteration cycle. In our case of fluctuating values, we take a weighted mean of the last four measured values, where the weight corresponds to the relative difference with respect to the unweighted mean value.

In the Lehmann representation, Eq. (7), only the states with one electron added (removed) relative to the ground state (GS) contribute to the first (second) term. Thus, in the following we refer to the states with one electron more (less) relative to the GS by electron (hole) states and denote the terms of the GF correspondingly.

In the special case of half-filling $n_{\text{imp}} = n = 1$, the condition for the occupation is always fulfilled, such that

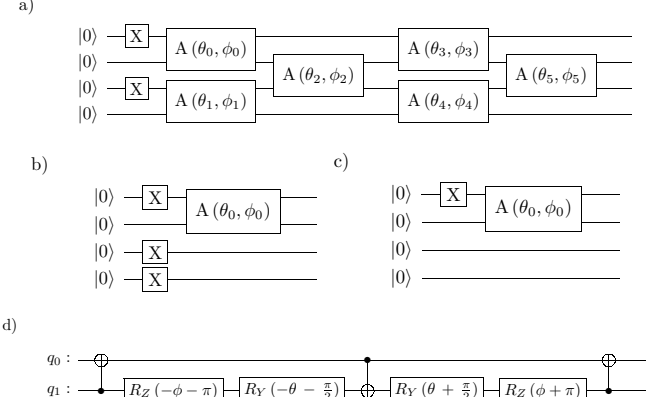


FIG. 2. Quantum circuits used for the computation of (a) the ground state, (b) electron states with spin up, and (c) hole states with spin up. (d) Decomposition of the A-gate into single qubit rotations and CNOT gates.

only the inner optimization loop for V has to be performed. In this case, $\mu = \varepsilon_c = U/2$, the electron (hole) states are those with $N = 3$ ($N = 1$) electrons in total, and the problem can be solved analytically [29]. The exact solution for the self-energy at half-filling reads

$$\Sigma(\omega) = \frac{U}{2} + \frac{U^2}{8} \left(\frac{1}{\omega - 3V} + \frac{1}{\omega + 3V} \right) \quad (11)$$

and the hybridization strength is given by

$$V = \begin{cases} \sqrt{M_2^{(0)}} - \frac{U^2}{36} & \text{for } U < U_c \\ 0 & \text{else,} \end{cases} \quad (12)$$

with the critical interaction parameter $U_c := 6\sqrt{M_2^{(0)}}$ indicating a Mott-insulator transition. For $U < U_c$ the system is metallic with two singularities of the self-energy at $\omega = \pm 3V$. When U approaches U_c from below, the two singularities move closer towards $\omega = 0$, until they meet at $U = U_c$ so that the system becomes insulating due to the strong interactions between the electrons for $U > U_c$. The analytic solution for the quasi-particle weight at half-filling is given by

$$z = \begin{cases} 1 - \left(\frac{U}{U_c} \right)^2 & \text{for } U < U_c \\ 0 & \text{else.} \end{cases} \quad (13)$$

III. QUANTUM COMPUTING APPROACH

We want to perform the most demanding task of DMFT calculations on a QC, namely the determination of the impurity GF G_{imp} . We use the Jordan Wigner transformation [31] for the mapping between the

Fermionic creation/annihilation operators and the Pauli spin operators

$$c_i^\dagger = \frac{1}{2} \left(\prod_{j=1}^{i-1} \sigma_j^z \right) (\sigma_i^x - i\sigma_i^y) \quad (14)$$

and

$$c_i = \frac{1}{2} \left(\prod_{j=1}^{i-1} \sigma_j^z \right) (\sigma_i^x + i\sigma_i^y), \quad (15)$$

with σ_i^x , σ_i^y , σ_i^z denoting the x , y , z Pauli operators, respectively. By this transformation we assign each orbital of the model to one qubit in the following order: $(d_\uparrow, c_\uparrow, d_\downarrow, c_\downarrow) \rightarrow (q_0, q_1, q_2, q_3)$. With this mapping, the AIM Hamiltonian (Eq. (2)) is written in terms of Pauli operators as

$$\begin{aligned} H = & \mathbf{I} \left(\frac{U}{4} + \varepsilon_d + \varepsilon_c - 2\mu \right) - (\sigma_1^z + \sigma_3^z) \left(\frac{\varepsilon_c}{2} - \frac{\mu}{2} \right) \\ & - (\sigma_0^z + \sigma_2^z) \left(\frac{U}{4} + \frac{\varepsilon_c}{2} - \frac{\mu}{2} \right) \\ & + \frac{V}{2} (\sigma_0^x \sigma_1^x + \sigma_2^x \sigma_3^x + \sigma_0^y \sigma_1^y + \sigma_2^y \sigma_3^y) \end{aligned} \quad (16)$$

As mentioned above, we will consider the special case of half-filling for which the parameters $\varepsilon_d = 0$ and $\varepsilon_c = U/2 = \mu$ [29]. The corresponding Hamiltonian reads

$$H = \frac{V}{2} (\sigma_0^x \sigma_1^x + \sigma_2^x \sigma_3^x + \sigma_0^y \sigma_1^y + \sigma_2^y \sigma_3^y) + \frac{U}{4} \sigma_0^z \sigma_2^z. \quad (17)$$

Note that in this special case of half-filling V is determined via Eq. (12) which leaves one free parameter U .

In order to solve the AIM for the ground state we employ a hybrid quantum-classical variational quantum eigensolver (VQE) algorithm [32]. In this approach we measure the expectation value of the Hamiltonian with respect to a parameterized state $|\psi(\{\theta_i\})\rangle$ with the help of a quantum computer. This expectation value serves as cost function of a classical optimizer, which is used to optimize the set of parameters $\{\theta_i\}$ until the cost function is minimal, which is then identified as the ground state energy of the system according to the variational principle. The quantum state is generated by a set of unitary gates, called the ansatz, which are executed on the qubits representing the system. For the ground state of the two-site AIM around half-filling we choose the particle-number conserving ansatz presented by Gard et al. [33] which is depicted in Fig. 2. In this ansatz, 12 real parameters are required to cover the whole Hilbert space of two electrons in four spin-orbitals. The respective quantum circuit which is capable of generating any state in this 12-dimensional Hilbert space is shown in Fig. 2 (a). It makes use of a so-called A-gate, which can be decomposed into elementary single and two-qubit gates [33], as

shown in Fig. 2 (d). Due to the normalization and an irrelevant global phase factor, two parameters and thus one A-gate can be removed. Further, as the Hamiltonian is symmetric under time reversal, all the ϕ parameters can be set to zero. Using the S_z -symmetry of the Hamiltonian, even the θ parameters of gates connecting both spin sectors can be fixed to zero, such that an optimization of only four parameters (θ_0 , θ_1 , θ_3 , and θ_4 in Fig. 2 (a)) is sufficient.

For the calculation of the GF in Eq. (7) we need to compute the excited states with one electron added or removed in comparison to the ground state. For the two-site DMFT model close to half filling the excited states are those with 1 or 3 electrons in the system, leading to four states that need to be determined in each case. As the Hamiltonian is spin-conserving and an uneven number of electrons is in these states, they can be sorted by their spin into two sets of two states. With the particle- and S_z -conserving ansatz (see Figs. 2 (b) and (c)) based on Ref. [33] we determine the lowest energy state by VQE for $+H$ and the highest energy state by VQE for $-H$ in each spin subspace. So far, 8 parameters are required to cover the whole Hilbert space, which can be further reduced to 3 due to normalization, global phase and time-reversal symmetry. As one spin-sector is always completely empty (filled) no gate is required for this sector and the entanglement between both sectors. Thus, only one parameter (θ_0), needs to be optimized by the VQE algorithm for these excited states.

We quantify the quality of the results of the quantum computation by comparison with the exact results that can be obtained by an exact diagonalization (ED) method. The comparison of eigenstates is done via the fidelity defined as

$$f = \left| \left\langle \Psi_{N,m}^{\text{ED}} | \Psi_{N,m}^{\text{VQE}} \right\rangle \right|^2 \quad (18)$$

where we transformed the VQE state $|\Psi_{N,m}^{\text{VQE}}\rangle$ into a vector in the Fock basis and project it on the eigenvector of the Hamiltonian $|\Psi_{N,m}^{\text{ED}}\rangle$, which we obtained by exact diagonalization.

With the circuits (Fig. 2) and VQE-optimized parameters at hand, that are needed to prepare the states in Eq. (7), we proceed to the calculation of the transfer matrix in the numerator. Exploiting the inversion of the Jordan-Wigner transformation, i.e. $\prod_{i=0}^{k-1} (\sigma_i^z) \sigma_k^x = (c_k + c_k^\dagger)$, we obtain

$$\begin{aligned} \left\langle \Psi_{N-1,m} \left| \left(\prod_{i=0}^{k-1} \sigma_i^z \right) \sigma_k^x \right| \Psi_{N,n} \right\rangle \\ = \langle \Psi_{N-1,m} | c_k | \Psi_{N,n} \rangle \quad (19) \end{aligned}$$

and a similar expression for the creation operator with respect to the states $|\Psi_{N+1,m}\rangle$, as the other term vanishes due to the fixed particle number. Thus, it is sufficient to measure only one term on the QC. That is, we combine the ground state circuit, Fig. 2 (a), the circuit

realization of the product of σ_i^z and σ_k^x operator and the inverse circuit of the excited state. Then, the transition probability is the probability of measuring the combined circuit in the state with all bits equal to zero.

IV. NOISE MODELS AND ERROR MITIGATION

We have tested the implementation of our algorithm using different simulators as implemented in QISKit [34] as well as real quantum computing devices. We refer to the linear algebra-based noiseless simulator as the *state vector simulator*. This simulator is used to verify that the algorithm is capable to obtain the correct solution.

The probabilistic simulator, which takes into account the stochastic nature of the quantum mechanical measurement process is referred to as the *QASM simulator* (quantum assembly language) [34]. Here, the decisive quantity which determines the quality of the result is the number of shots, i.e. the number of repetitions of the calculation from which the probability distribution of an observable and finally its expectation value are deduced.

Furthermore, we use a noisy simulator which captures measurement errors, single- and two-qubit gate errors, depolarization, and thermal-relaxation errors. We construct this *fake backend simulator* by using the information of the IBMQ Ehninghen device. We also construct fake backends with rescaled error parameters.

A VQE calculation requires the choice of an optimization algorithm. Here we use QISKit's implementation of the limited-memory Broyden-Fletcher-Goldfarb-Shannon optimization algorithm (L_BFGS_B) for the state vector simulator and in all other cases the simultaneous perturbation stochastic approximation (SPSA) optimizer [35], which is an optimizer adapted to cope with noisy data.

When running our VQE algorithm on the fake backend simulator or on real hardware, we use error mitigation to address the issue of state-preparation-and-measurement (SPAM) errors. In a pre-processing step we compute the probabilities for preparing the register in one state and thereafter measuring another. This set of probabilities defines a matrix which can be inverted to perform error mitigation on the measured population counts of a quantum calculation. We use the SPAM error mitigation as implemented in the M3 package of QISKit [36].

V. RESULTS

In this section we proceed along the sequence of different steps in the DMFT self-consistency loop and discuss the results obtained using different levels of noise as outlined above. This, in detail, comprises the determination of the different states and their energies by VQE, the calculation of the GF in the Lehmann representation and thus the transition probabilities, the determination of the

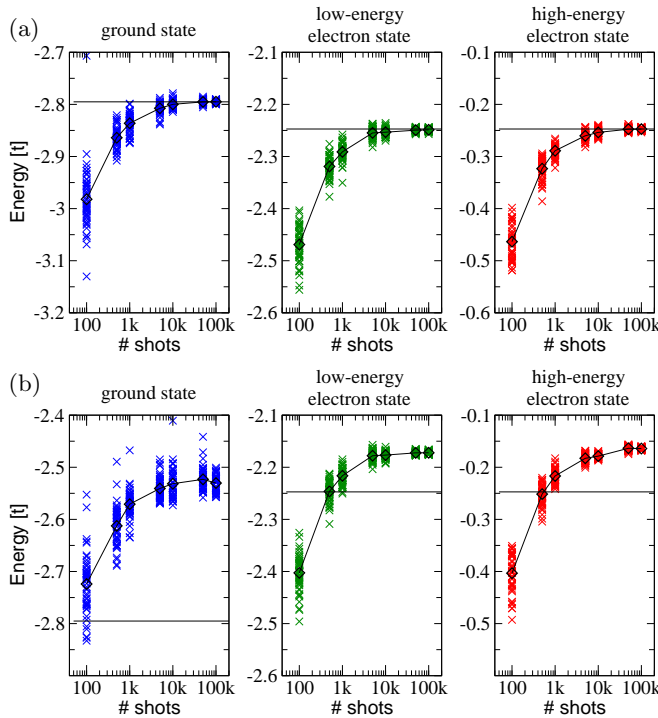


FIG. 3. Convergence of energies based on VQE as a function of the number of shots, using (a) the QASM simulator and (b) a fake backend. Shown are results for the ground state with $N = 2$, and the low- and high-energy electron spin-down states ($N = 3$, $S_z = -1$). The diamond symbols connected by lines represent the mean calculated from 50 runs, while the cross symbols refer to the result of individual runs. Horizontal solid black lines indicate the exact eigenenergies.

quasi-particle weight and finally the full self-consistent solution.

A. Energy Spectrum

We consider the two-site DMFT model at half-filling with $\varepsilon_a = 0$, $\varepsilon_c = U/2 = \mu$ and V according to Eq. (12). In the first step, we determine the eigenstates (eigenenergies and eigenvectors) required for the Lehmann representation of the GF by VQE optimization using ansatz circuits with $N = 2$ and $S_z = 0$ for the global ground state and for all the states in the $S_z = \pm 1$ subspaces for $N = 1$ and $N = 3$ as described in Sec. III.

The eigenenergies obtained by using our QC approach with the state vector simulator and the L_BFGS_B optimizer agree with those from exact diagonalization of the Hamiltonian up to $10^{-8} t$. In addition, the states obtained by VQE have a fidelity close to 1 with respect to the exact eigenstates. Thus, the chosen ansatz states with the parameters obtained from VQE are well suited to reliably obtain the states of the system required for the GF.

Next, we perform the VQE optimization employing the

probabilistic QASM simulator with a finite number of shots. Here we use the SPSA optimizer. By increasing the number of shots, the measured energies are expected to become more and more precise, as the stochastic accuracy grows with the number of shots N by $\propto \sqrt{N}$, so that the optimizer should improve in finding the correct states. In the limit of an infinite number of shots we should, thus, recover the exact results as obtained by exact diagonalization or with the state vector simulator. We performed the VQE optimization 50 times for each chosen number of shots for all the states. This allows to average out the effect of the stochastic noise and the stochastic nature of the SPSA optimizer.

Figure 3 (a) shows the evolution of the minimal measured eigenvalues in the optimization with the shot number for the GS, one low-energy electron, and one high-energy electron state. When the number of shots is increased, the accuracy of the results is improved and the spread of the results is significantly reduced. The surprisingly small values for a small number of shots, which are even below the exact ground state of the system, result from the statistical fluctuations and our choice of criteria to determine the best parameters. The SPSA optimizer as implemented in QISKit returns the last parameters accepted, even if at some point in the optimization history smaller cost values were obtained. Therefore, we tracked all intermediate results and then took the overall lowest cost values with their corresponding parameters. For a small number of shots, strong statistical fluctuations lead to eigenvalues, which might be even below that of the ground state. As we collected about 200 values for the cost function, we have a large chance to choose such a statistical outlier as our optimal value, so that we sample the lowest branch of the curve which is proportional to \sqrt{N} for the expectation values. When the number of shots is increased, the statistical fluctuation is reduced, and thus we obtain expectation values matching the ground state. From this analysis we conclude that at least $10k$ shots are required to obtain reasonable and reliable results.

In order to investigate how much the errors of a real backend influence the results of successful QC calculations, we performed the same VQE simulations (SPSA optimizer, 200 iterations) with a fake backend based on the real error-rate data available for the IBMQ Ehningen [37] and M3 error mitigation. In Fig. 3 (b) we show the resulting energies for 50 VQE runs per shot number. The curves show the same trend as those of the QASM result, however, they converge to values deviating from the exact ones by about 10 % and 5 % for the GS and the electron state, respectively, due to the simulated device errors. The SPAM errors, which are dominant in short circuits, are well reduced by the M3 error mitigation, the mainly remaining errors are the CNOT errors. As the ground state circuit contains 15 CNOT gates compared to 3 CNOT gates for the electron state circuit, it is significantly more affected by the CNOT error, leading to the larger error in the resulting expectation value.

We compare these results with results of VQE calculations on the real backend IBMQ Ehningen using the same setting but a reduced variation in the number of shots due to the limited computer-access time. In Figs. 4 (a) and (b) we observe a similar behavior for the expectation value of the GS and electron spin-down state as observed with the fake backend. The absolute values obtained from the real backend and those from the fake backend agree well, regarding the natural statistical fluctuations within $0.1 t$ for both states. This indicates, that the fake backend mimics the behavior of the real backend reasonably well.

To analyze the accuracy of the resulting state, we calculate the exact expectation values corresponding to the optimal parameters determined in the respective VQE runs. The resulting expectation values, shown in Figs. 4 (c) and (d), are significantly improved compared to the evaluation on the quantum hardware in both cases. For the electron state, we observe a convergence to the exact value with $10 k$ shots. This indicates that the presence of noise is leading to a systematic offset in the one-dimensional energy landscape during the VQE optimization. For the GS the exact expectation values corresponding to the obtained optimal parameters have, in most cases, an error of less than 5 %. Thus, in the presence of CNOT errors and statistical noise, although the optimizer is not able to find the global minimum in the 4-parametric energy landscape, at least it leads to a state close to it. Its quality is actually much better, than we would expect based on the expectation value obtained from the device.

Based on the results above, we have to perform our calculations with at least $10 k$ shots in order to reduce shot noise to a tolerable level. While M3 mitigates SPAM errors very well, the CNOT errors are a significant threat to obtain accurate results on the real hardware. We will further investigate their effect in Sec. V E. However, in order to go through the steps of our DMFT algorithm, we first discuss the computation of the GF with respect to stochastic errors in the following section.

B. Green's function

According to Eq. (7), the GF of the two-site DMFT model has a four-peak structure where the peaks at negative frequencies originate from hole excitations and those at positive frequencies from electron excitations. Their positions are determined by the corresponding energies relative to the ground state energy and their shapes by the transition rates. Due to the electron-hole symmetry of our model at half-filling, the GF is symmetric with respect to $\omega = 0$. As the inverse GF and its free counterpart appear in the Dyson equation (9), the self-energy has poles at energies where only one of the two GFs is zero as the divergences cancel otherwise. While the free GF has a single zero crossing, the full GF has three of which one is the same as the one of the free GF, so that

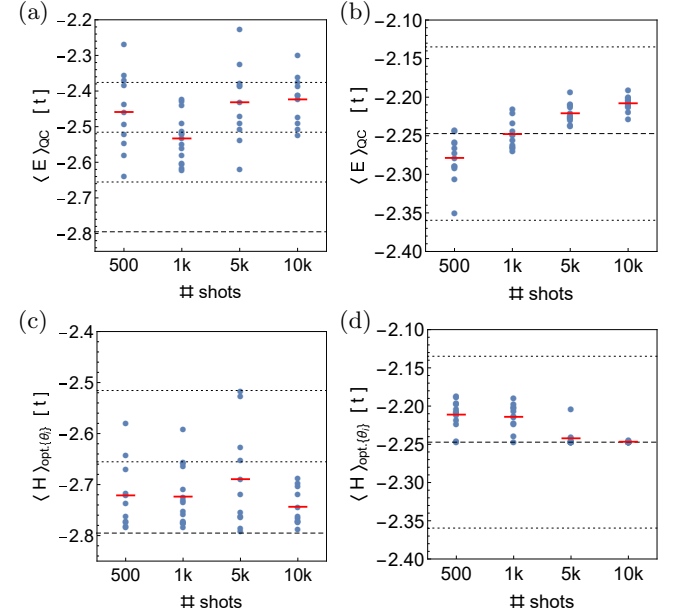


FIG. 4. Expectation values for the energy of (a) the ground state and (b) the low-energy electron spin-down state obtained by independent VQE simulations on IBMQ Ehningen for different numbers of shots. The blue points correspond to ten individual runs each and the red lines to their mean value. In (c) and (d) we show the exact energy expectation values corresponding to the optimal parameters found in the VQE runs of (a) and (b), respectively. The dashed black horizontal lines indicate the exact value and the dotted lines deviations in steps of 5 %.

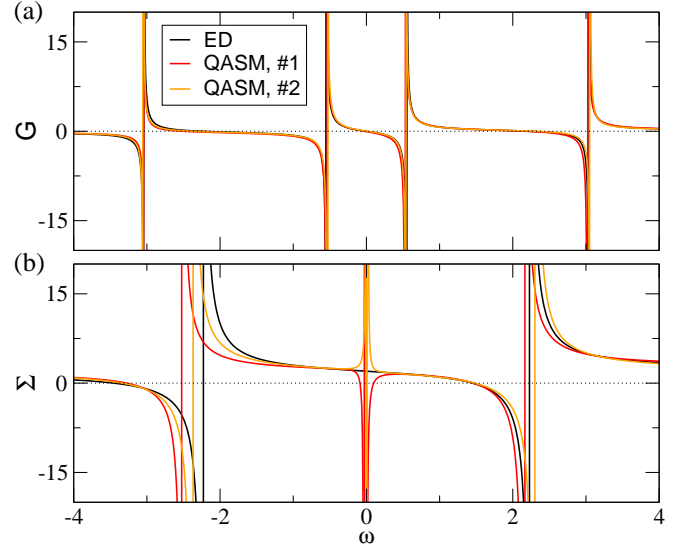


FIG. 5. Impurity GF (a) and self-energy (b) for the half-filled two-site DMFT model with $U = 4t$. The exact diagonalization (ED) and state vector VQE result are in perfect agreement and we only show the ED result. The two runs using the QASM simulator with $10 k$ shots for the VQE optimisation and transition rates illustrate the difficulties arising from inaccurate QC results.

the self-energy finally has two singularities and preserves the electron-hole symmetry.

When energies obtained by VQE calculations with the state vector simulator are used to construct the impurity GF and the self-energy for $U = 4t$, a perfect agreement is achieved with the exact quantities obtained from exact diagonalization (cf. Fig. 5). This could be expected by the high precision in energies and the high fidelities, compared to the exact results, as discussed in the previous section. Thus, the high fidelity leads to transition rates which are also in very good agreement with the exact values. To obtain the derivative of the self-energy at $\omega = 0$ independent of small numerical fluctuations we use the first coefficient of a linear fit to its curve in the proximity to this frequency. Thereby we obtain the quasi-particle weight by Eq. (10) as $z = 0.5552$ which is very close to the exact value of $z_{\text{ex}} = 0.5556$.

When we use the results from stochastic QASM simulations, the constructed GFs differ only slightly for at least $10k$ shots while there are larger differences observable in the self-energy (see Fig. 5). This results from the imprecision in the VQE calculation of the eigenstates. While deviations in the eigenenergies shift the poles of the GF, the eigenvectors influence the transition rates, which are relevant for the curvature of the GF. Furthermore, the errors on the eigenstates lift the electron-hole symmetry. In total, the zeroes in the GF are shifted, resulting in corresponding shifts of the peaks in the self-energy. Most crucially, the coincidence with the zeroes of the free GF is lost. This results in a two-peak structure close to $\omega = 0$ which prevents us from taking the derivative of the self-energy (cf. Eq. (10)) at this point. In addition, the shift of the other peaks has an influence on the curvature at that point, too. Figure 5 exemplarily shows this for two runs with $10k$ shots. We observed that even $100k$ shots are not sufficient to get rid of this artificial two-peak structure at $\omega = 0$.

A possible approach to overcome these unphysical quasi-particle signatures follows a regularization procedure as first suggested in Ref. [21]. Here, the transition rates and energies are corrected such that the zeroes and the derivative of the impurity GF matches those of the free GF at the bath energies ε_c . However, we do not follow this route here, as for some test cases the correction terms were significantly larger than the measured values and sometimes lead to unphysical results with negative transition rates.

Thus, we propose to take a more pragmatic route and fit a function of the form $a \cdot \tan(\omega) + b \cdot \omega + c$ to the self-energy in the region between the two physical peaks. This function was chosen because the Taylor expansion around $\omega = 0$ of the analytic self-energy consists only of odd-integer exponents similar to the expansion of the tangent. We refer to it in the following as the tan-fit approach. For the fitting procedure we exclude an interval containing the peaks around $\omega = 0$ which should cancel due to the coincidence of zeroes of both GFs. The quasi-particle weights can now be obtained from the derivative of the

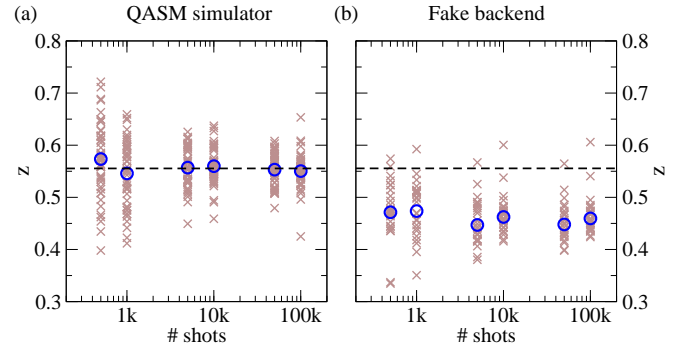


FIG. 6. The quasi-particle weight z obtained via the tan-fit procedure applied to the self-energies as function of the number of shots. The self-energy is calculated for the two-site DMFT system at half-filling and $U = 4t$ with the analytic exact V with (a) probabilistic QASM simulations and (b) a fake backend. Due to the stochastic nature, we performed 50 runs (gray crosses) and show their arithmetic mean (blue circles). The exact value for this parameter setting is marked by the dashed black lines.

fitting function at $\omega = 0$. We test this approach for the exact self-energy and obtain the quasi-particle weight 0.542 that is reasonably close to the exact value of $z_{\text{ex}} = 0.555$.

In Fig. 6 (a) we display the quasi-particle weights obtained by this tan-fit procedure applied to the self-energies obtained with a finite number of shots. The determined quasi-particle weights are spread around the exact values. When the number of shots is increased, the spread is reduced, which agrees well with the more accurate results in this case described above. However, even for $100k$ shots the results of individual runs differ from the exact value by up to 10%.

When we use a fake backend with a noise model based on data taken from the real system IBMQ Ehningen [37], we obtain the quasi-particle weights displayed in Fig. 6 (b) from the tan-fit approach. While the spread of the individual results reduces with a larger number of shots, the quasi-particle weight is always about 15% smaller than the exact one. Tracing back this systematic deviation, we turn back to the construction of the GF. As the eigenvalues obtained by VQE always tend to too small values, the peaks of the noisy GF move towards $\omega = 0$ and so do the zero transitions. By this, the peaks in the self-energy are at too small frequencies. As the tan-fit targets the interval between them, their closeness leads to a too large slope and thus to too small quasi-particle weights.

Due to limited resources we performed the full set of VQE calculations and transition-rate measurements on the state-of-the-art QC IBMQ Ehningen only 5 times with $10k$ shots. The resulting GF and self-energies of three of them are displayed exemplarily in Fig. 7. The GFs in plot (a) show the shift of the peaks towards $\omega = 0$ due to the imprecision in the energies obtained by VQE and, thus, of the zero-transition. The latter is also af-

run #	1	2	3	4	5
z	0.507	0.528	0.387	0.460	0.484

TABLE I. z -values obtained by the tan-fit approach applied to five self-energies obtained from independent calculations on the IBMQ Ehninghen.

fected by the transition rates, whose measurement results in errors of up to 25 % with respect to an analytic evaluation. Figure 7 (b) shows the effect of these inaccuracies on the self-energy. The single-peak or double-peak structures close to $\omega = 0$ result from the missed cancellation of zero-transitions in the free and impurity GF, as described above. The peaks of the self-energy on the other hand are shifted away from their original position. As the tan-fit performs a fit between these two peaks, their position has an influence on the slope at $\omega = 0$. Performing this fit, we obtain the values listed in Tab. I, where we see a surprisingly good agreement with the exact value when the shift is only small as in the apparently good QC-run # 2. However, the obtained value significantly deviates for the particularly bad run QC # 3. The results of the real backend qualitatively are in line with those obtained from the fake backend presented before, cf. Fig. 6 (b).

C. Resources

Based on the previously reported calculations we estimate the computational costs for a complete self-consistent calculation of the GF on a QC using the Lehmann representation. The Hamiltonian of the model consists of three qubit-wise non-commuting sets of Pauli strings. Thus, for one expectation value we need to run the quantum circuits with measurements in each corresponding basis (cf. Fig. 2). Therefore the number of circuits to be performed is three times the number of shots.

We estimate the respective run time of one circuit by using approximate execution times from current IBMQ devices. Two-qubit gates require about 400 ns and the readout and measurement takes 700 ns while single qubit gates are sufficiently fast or even virtual such that we do not take them into consideration. Assuming parallel execution of CNOT gates and readout, the execution of the ground state quantum circuit consisting of 9 layers of CNOT gates requires about 4.3 μ s. As currently the state preparation is achieved by thermalization of the system, between two circuit executions a waiting time is required, which is of the same order as the system's T_1 time. As this is about 150 μ s for the IBM systems, this is the dominating time scale for the calculations we consider in the following. Therefore, one expectation value with 10 k shots requires about 4.5 s instead of 0.13 s for the plain circuits. In practice, however, we observed average run times of about 20 s using the IBM runtime sampler, indicating an overhead that we did not address in our considerations.

The hybrid algorithm presented in Sec. II requires one

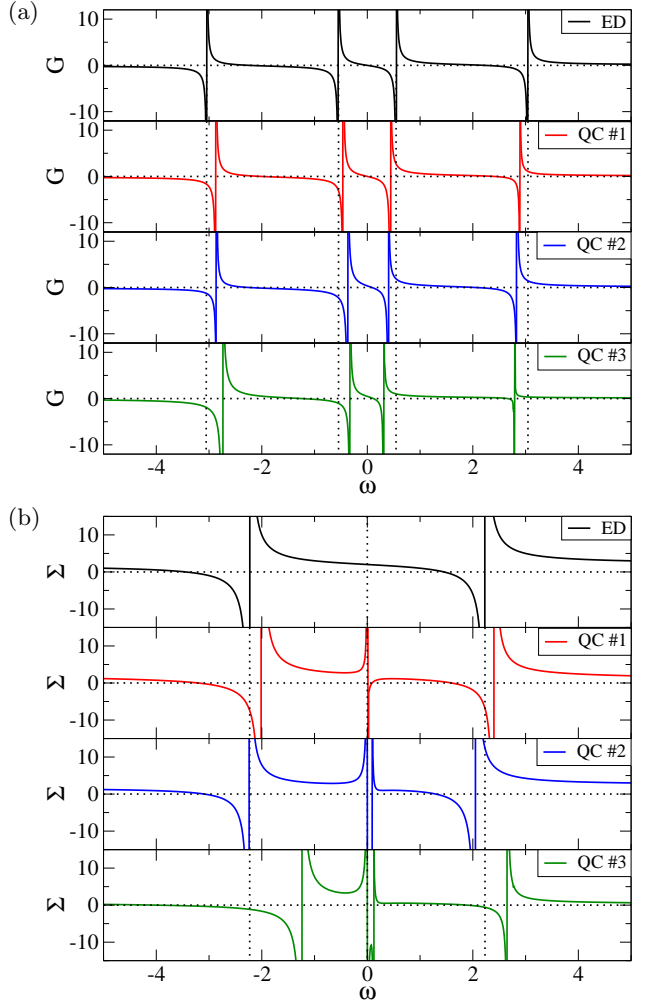


FIG. 7. (a) Impurity GF and (b) self-energy at half-filling at the self-consistent condition with $U = 4t$ obtained from three numerical experiments on IBMQ Ehninghen and compared to the exact result (ED). The VQE calculation was performed with the SPSA optimizer, 10 k shots and M3 readout error mitigation.

VQE calculation for the ground state and eight VQE calculations for the excited states in the case of the two-site DMFT model, in each step, if no symmetries are exploited or present. For the VQE runs with stochastic noise and the SPSA optimizer (cf. Sec. V A) we observed a convergence after 170 to 300 iterations for the GS and after about 100 iterations for the excited states. However, on a real device our convergence criterion did not lead to an end of the optimization process, such that 250 cost function evaluations were performed in total. The measurement of these 250 eigenvalues thus requires about 90 minutes on the real device, while the plain circuit execution requires only about half a minute (32.5 s).

The self-consistent DMFT loop for the optimization of the hybridization requires in the best case, using the state vector simulator and BFGS optimizer, 10 to 30 iter-

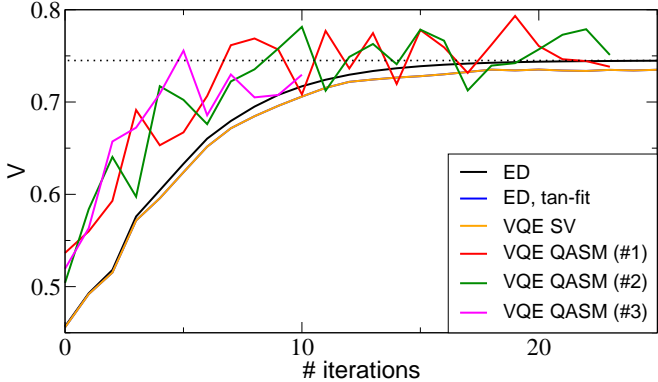


FIG. 8. Convergence of the hybridization V in the DMFT self-consistency loop at half filling, $U = 4t$ and initial value $V_{\text{init}} = 0.4t$ using different variants to solve the AIM. While for the curve "ED" the numerical derivative at $\omega = 0$ was taken, the tan-fit approach was used in all other cases. The VQE results were obtained with either the state vector simulator and L_BFGS_B optimizer (SV) or with the QASM simulator and SPSA optimizer using $10k$ shots.

ations, depending on the interaction strength, until self-consistency is reached up to an accuracy of $5 \cdot 10^{-3}t$. Thus, a total of 90 to 270 VQE optimizations are required, which in the best case would lead to a computation time of 135 h on a real device, while the pure circuit execution time (without state preparation) is less than an hour (49 min). As we do not have access to sufficient compute time on quantum computers, we investigate our self-consistent hybrid algorithm on simulated or fake backends (cf. Sec. V D) in the following.

D. Self-Consistency Loop

We use our VQE based approach to obtain a self-consistent solution of the two-site DMFT model at half filling, i.e. we perform the inner optimization loop as displayed in Fig. 1. Figure 8 demonstrates the convergence of the hybridization strength at half filling and $U = 4t$ for different solvers starting from an initial value $V_{\text{init}} = 0.4t$ towards the exact value of $V_{\text{exact}} = 0.745t$. For exact diagonalization, the positions of zeroes of both GFs perfectly agree, such that the respective divergences in the self energy cancel and the slope of Σ at $\omega = 0$ can be numerically determined accurately. Thus, V smoothly converges to the exact value with a threshold of $10^{-3}t$. When we use this solver but apply our tan-fit approach to obtain the quasi-particle weight, the hybridization converges in the same way to a value of $0.734t$ which matches the exact value within 1.5%. The convergence is the same in the case of our quantum circuit based approach with the state vector simulator and the L_BFGS_B optimizer, such that both graphs overlap in Fig. 8.

The convergence for three different runs with the QASM simulator using $10k$ shots is also shown in Fig.

8. Although the values fluctuate strongly, the curve converges towards the correct values for all runs. This behavior is achieved by our mixing scheme based on weighted means, as described after the iteration loop in section II.

E. Mott metal-insulator transition

Motivated by these results we investigate the Mott metal-insulator transition of the two-site DMFT model at half filling. Figure 9 shows how the quasi-particle weight z evolves with the interaction strength U for the different approaches investigated from finite values in the metallic phase for $U < U_c = 6t$ to the Mott-insulating phase for $U > U_c$.

Overall, exact diagonalization in combination with the tan-fit approach reproduces the quasi-particle weight over the whole U -range very well in comparison to the analytic result [29]. Although it tends to overestimate z in the metallic region close to the Mott transition, it still reproduces a sharp transition, however at a slightly larger U value. Simulations using the state vector simulator exactly reproduce the ED results.

With the QASM simulator we performed ten independent self-consistent DMFT simulations for each U -value using either $1k$, $10k$, or $100k$ shots. In Fig. 9 (b)-(d), we show both, the individual results (crosses) as well as the mean result of all these runs (blue line) together with the analytic result (black line). With $1k$ shots we were able to reproduce the curve only for $U < 4t$ while we failed to obtain the Mott transition. Calculations with $10k$ or $100k$ shots resulted in a much better agreement over the whole U -range and (for most runs) a vanishing z for the insulating phase. However, here we get a smooth transition instead of a sharp edge at $U = 6t$. Despite this most challenging feature our pragmatic approach can overcome the limitations of noisy data obtained on a NISQ computer.

For the next step towards an implementation on real QC hardware, we performed simulations of the phase diagram with a fake version of the IBMQ Ehning [37] using $10k$ shots. Using the fake backend with the full noise model we reproduce the behavior in the weak coupling regime, but fail to reproduce the transition to the insulating phase, cf. left panel of Fig. 10. In order to investigate the influence of noise on the results, we created fake backends with scaled noise. By a scale factor of 0.1 and 0.01 we refer to a scaling of gate and SPAM noise by a factor of 0.1 and 0.01 and an elongation of the coherence times T_1 and T_2 by a factor of 10 and 100, respectively. Performing the simulation with a noise factor of 0.1, the phase diagram is well captured, although the z -values are systematically underestimated. This is most probably due to the systematic overestimation of the eigenenergies, which shift the peaks of the self-energy closer to $\omega = 0$. Finally, by scaling the errors by a factor of 0.01, the phase diagram can be reproduced very well. However, as in the previous cases, our approach does

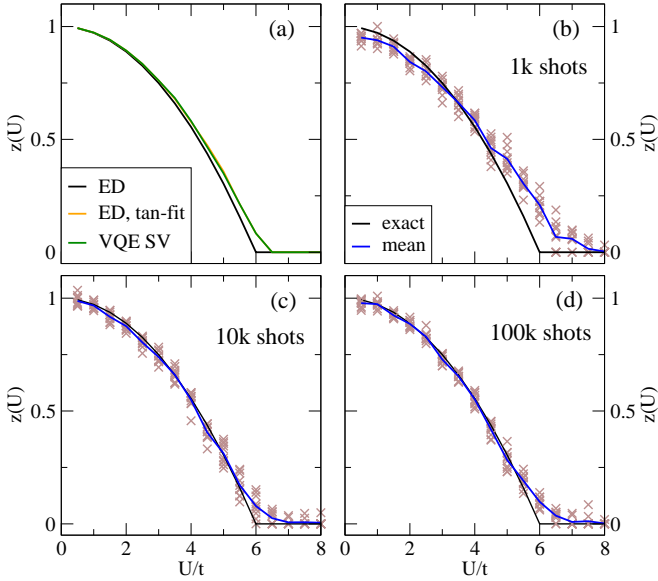


FIG. 9. (a): Dependence of the quasi-particle weight z on the interaction strength U obtained from a self-consistent DMFT cycle when using exact diagonalization without (ED) and with the tan-fit (ED + tan-fit) and the VQE solver with the state vector simulator (VQE SV). (b)-(d): Same as (a) but with the QASM simulator and 1 k , 10 k and 100 k shots, respectively. The crosses mark the final values of 10 individual runs, while the blue lines mark their arithmetic mean values in comparison to the analytic result (black line).

not give the sharp Mott transition. Note that even in this case statistics are required and the good agreement of the displayed curve with the exact result is obtained from averaging individual data point with a spread as indicated by the error bars.

VI. CONCLUSION

In this paper we investigated the application of a quantum computer to obtain the Green's function of a fermionic quantum system through its Lehmann representation. Explicitly, we considered the two-site DMFT model at half-filling. However, our approach is more general and does not rely on using two sites only or the constraint of particle-hole symmetry. We used the VQE approach to determine the relevant eigenstates and transition rates without exploiting any symmetry. By calculations with (i) only stochastic noise, (ii) simulated device noise, and (iii) on a real IBMQ machine we extracted three main obstacles for full self-consistent DMFT calculations on state-of-the-art quantum computers based on this approach:

(1) The limited accuracy of the expectation values of the eigenenergies and transition rates already resulting from statistical noise leads to an unphysical two-peak structure in the self-energy on the real frequency axis, explicitly around $\omega = 0$. As this prohibits the determi-

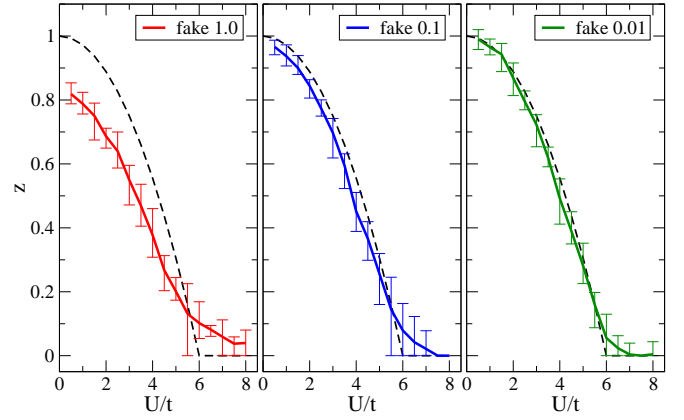


FIG. 10. Quasi-particle weight obtained from full self-consistent two-site DMFT simulations with fake backends based on the error rates and coherence times of IBMQ Ehningen without scaling (fake 1.0), with scaling by a factor of 0.1 (fake 0.1) and a factor of 0.01 (fake 0.01). The solid lines mark the arithmetic mean values of ten runs, and the bars indicate the maximum and minimum of the obtained values. The exact result is shown as black dashed line.

nation of the quasi-particle weight from the derivative, we introduced a fitting approach to cure the artificial two-peak structure enclosing $\omega = 0$. By self-consistent calculations we showed that this approach is able to reproduce the correct phase diagram of the model including the Mott transition, even in the presence of shot-noise with at least 10 k shots. We note that there are alternative approaches for the determination of the quasi-particle weight, like calculations in Matsubara frequencies or using the Kramers-Kronig relation to convert it into an integral over the imaginary part of the self-energy [19].

(2) The device noise, like SPAM, dephasing and CNOT errors, leads to even less accurate results. While the fitting procedure introduced above can overcome the more pronounced two-peak structure around $\omega = 0$, its results are always too low, as even the physical peaks of the self-energy are shifted. Therefore, by performing self-consistent simulations with scaled noise of a real backend, we demonstrate that the noise rates of current quantum computers have to be improved by an order of magnitude in order to obtain numerical results with acceptable accuracy.

(3) A self-consistent calculation on real quantum hardware based on the Lehmann representation requires a large amount of quantum resources which is currently not available. For the two-site DMFT model these are 9 VQE simulations and the calculation of 8 transition matrix elements for the calculation of one GF, which requires several hours on current QC hardware. As this is necessary in each of the at least 10 iterations of the DMFT self-consistency loop, it would run for several days, unless a parallel execution of the VQE were possible. For more complex systems, a solver for excited states is needed,

as $\binom{N}{n+1} + \binom{N}{n-1}$ electron and hole states have to be determined for a system with N orbitals and n electrons in the ground state. The variational quantum deflation method [38] has an exponential scaling and can not be parallelized, as the determination of the m th state requires the calculation of the overlap with all previously found $m-1$ other states in each VQE iteration. Contrary, the subspace search VQE method [39] scales exactly with the number of states required and is parallelizable, as one expectation value has to be calculated for each of the orthogonal input states with the same parameter set. On the other hand, semi-classical matrix-based approaches like quantum subspace expansion [40] or quantum equation of motion [28, 41] may even show a better scaling, as they require only one VQE optimization of the ground state and the measurement of transition matrix elements in a basis created by application of excitation operators to the ground state.

These points (1)–(3) suggest, that solving a DMFT model with satisfactory accuracy within a reasonable amount of computation time on a gate-based QC via the Lehmann approach is not feasible in the near future. Note that in contrast to our generally applicable approach, up to now all papers using the time-evolution

based approaches were tailored to the two-site DMFT model in the determination of the GF. The works of Keen et al.[19] and Kreula et al.[20] exploited the knowledge of the analytic form of the GF at half filling in order to obtain the amplitudes and frequencies of two cosine functions from a fit to the QC real time GF. The recent work of Steckmann et al. [25] is already more generally applicable as it comprises a flexible frequency extraction procedure, but the derivative-free determination of the quasi-particle weight still relies on particle-hole symmetry.

In conclusion, the development of noise-resilient and size-scalable algorithms and workflows to run meaningful self-consistent DMFT calculations for strongly correlated electron systems on noisy intermediate quantum computing hardware remains an open challenge for future work.

VII. ACKNOWLEDGMENTS

This work has been funded by the Ministry of Economic Affairs, Labour and Tourism Baden Württemberg through the Competence Center Quantum Computing Baden-Württemberg (KQCBW), projects QuEST and QuEST+.

[1] R. M. Martin, Electronic structure: basic theory and practical methods (Cambridge University Press, 2020).

[2] W. Metzner and D. Vollhardt, Correlated lattice fermions in $d = \infty$ dimensions, *Phys. Rev. Lett.* **62**, 324 (1989).

[3] A. Georges and G. Kotliar, Hubbard model in infinite dimensions, *Phys. Rev. B* **45**, 6479 (1992).

[4] P. W. Anderson, Localized magnetic states in metals, *Phys. Rev.* **124**, 41 (1961).

[5] A. Georges, G. Kotliar, W. Krauth, and M. J. Rozenberg, Dynamical mean-field theory of strongly correlated fermion systems and the limit of infinite dimensions, *Rev. Mod. Phys.* **68**, 13 (1996).

[6] K. Held, Electronic structure calculations using dynamical mean field theory, *Adv. Phys.* **56**, 829 (2007).

[7] G. Kotliar and D. Vollhardt, Strongly correlated materials: insights from dynamical mean-field theory, *Phys. Today* **57**, 53 (2004).

[8] G. Kotliar, S. Y. Savrasov, K. Haule, V. S. Oudovenko, O. Parcollet, and C. A. Marianetti, Electronic structure calculations with dynamical mean-field theory, *Rev. Mod. Phys.* **78**, 865 (2006).

[9] F. Nilsson and F. Aryasetiawan, Electronic structure of strongly correlated materials: from one-particle to many-body theory, *Mater. Res. Express* **4**, 034001 (2017).

[10] C. Watzenböck, M. Fellinger, K. Held, and A. Toschi, Long-term memory magnetic correlations in the Hubbard model: A dynamical mean-field theory analysis, *SciPost Phys.* **12**, 184 (2022).

[11] H. Chen, A. Hampel, J. Karp, F. Lechermann, and A. J. Millis, Dynamical mean field studies of infinite layer nickelates: Physics results and methodological implications, *Front. Phys.* **10**, 10.3389/fphy.2022.835942 (2022).

[12] M. Karolak, G. Ulm, T. Wehling, V. Mazurenko, A. Poteryaev, and A. Lichtenstein, Double counting in lda+dmft—the example of nio, *J. Electron Spectrosc. Relat. Phenom.* **181**, 11 (2010).

[13] G. Sangiovanni, A. Toschi, E. Koch, K. Held, M. Capone, C. Castellani, O. Gunnarsson, S. K. Mo, J. W. Allen, H. D. Kim, A. Sekiyama, A. Yamasaki, S. Suga, and P. Metcalf, Static versus dynamical mean-field theory of Mott antiferromagnets, *Phys. Rev. B* **73**, 1 (2006).

[14] C. Lupo, F. Jamet, W. H. T. Tse, I. Rungger, and C. Weber, Maximally localized dynamical quantum embedding for solving many-body correlated systems, *Nat. Comput. Sci.* **1**, 410 (2021).

[15] E. Y. Loh, J. E. Gubernatis, R. T. Scalettar, S. R. White, D. J. Scalapino, and R. L. Sugar, Sign problem in the numerical simulation of many-electron systems, *Phys. Rev. B* **41**, 9301 (1990).

[16] R. Žitko and T. Pruschke, Energy resolution and discretization artifacts in the numerical renormalization group, *Phys. Rev. B* **79**, 085106 (2009).

[17] B. Bauer, D. Wecker, A. J. Millis, M. B. Hastings, and M. Troyer, Hybrid quantum-classical approach to correlated materials, *Phys. Rev. X* **6**, 1 (2016).

[18] B. Jaderberg, A. Agarwal, K. Leonhardt, M. Kiffner, and D. Jaksch, Minimum hardware requirements for hybrid quantum-classical DMFT, *Quantum Sci. Technol.* **5**, 10.1088/2058-9565/ab972b (2020).

[19] T. Keen, T. Maier, S. Johnston, and P. Lougovski, Quantum-classical simulation of two-site dynamical mean-field theory on noisy quantum hardware, *Quantum Sci. Technol.* **5**, 10.1088/2058-9565/ab7d4c (2020).

[20] J. M. Kreula, S. R. Clark, and D. Jaksch, Non-linear quantum-classical scheme to simulate non-equilibrium strongly correlated fermionic many-body dynamics, *Sci. Rep.* **6**, 1 (2016).

[21] I. Rungger, N. Fitzpatrick, H. Chen, C. H. Alderete, H. Apel, A. Cowtan, A. Patterson, D. M. Ramo, Y. Zhu, N. H. Nguyen, E. Grant, S. Chretien, L. Wossnig, N. M. Linke, and R. Duncan, Dynamical mean field theory algorithm and experiment on quantum computers, (2019), [arXiv:1910.04735](https://arxiv.org/abs/1910.04735).

[22] S. Endo, I. Kurata, and Y. O. Nakagawa, Calculation of the Green's function on near-term quantum computers, *Phys. Rev. Res.* **2**, 1 (2020).

[23] R. P. Feynman, Simulating physics with computers, *Int. J. Theor. Phys.* **21**, 467 (1982).

[24] F. Libbi, J. Rizzo, F. Tacchino, N. Marzari, and I. Tavernelli, Effective calculation of the Green's function in the time domain on near-term quantum processors, *Phys. Rev. Res.* **4**, 1 (2022).

[25] T. Steckmann, T. Keen, E. Kökcü, A. F. Kemper, E. F. Dumitrescu, and Y. Wang, Mapping the metal-insulator phase diagram by algebraically fast-forwarding dynamics on a cloud quantum computer, *Phys. Rev. Res.* **5**, 023198 (2023).

[26] F. Jamet, A. Agarwal, C. Lupo, D. E. Browne, C. Weber, and I. Rungger, Krylov variational quantum algorithm for first principles materials simulations, (2021), [arXiv:2105.13298](https://arxiv.org/abs/2105.13298).

[27] F. Jamet, A. Agarwal, and I. Rungger, Quantum subspace expansion algorithm for Green's functions, (2022), [arXiv:2205.00094](https://arxiv.org/abs/2205.00094).

[28] J. Rizzo, F. Libbi, F. Tacchino, P. J. Ollitrault, N. Marzari, and I. Tavernelli, One-particle Green's functions from the quantum equation of motion algorithm, (2022), [arXiv:2201.01826](https://arxiv.org/abs/2201.01826).

[29] M. Potthoff, Two-site dynamical mean-field theory, *Phys. Rev. B* **64**, 1 (2001), 0107502.

[30] J. Hubbard, Electron correlations in narrow energy bands, *Proc. R. Soc. Lond. A* **276**, 238–257 (1963).

[31] P. Jordan and E. Wigner, Über das Paulische Äquivalenzverbot., *Zeitschrift für Phys.* **47**, 631 (1928).

[32] A. Peruzzo, J. McClean, P. Shadbolt, M. H. Yung, X. Q. Zhou, P. J. Love, A. Aspuru-Guzik, and J. L. O'Brien, A variational eigenvalue solver on a photonic quantum processor, *Nat. Commun.* **5**, 10.1038/ncomms5213 (2014).

[33] B. T. Gard, L. Zhu, G. S. Barron, N. J. Mayhall, S. E. Economou, and E. Barnes, Efficient symmetry-preserving state preparation circuits for the variational quantum eigensolver algorithm, *npj Quantum Inf.* **6**, 10.1038/s41534-019-0240-1 (2020).

[34] Qiskit contributors, (2023), qiskit: An Open-source Framework for Quantum Computing, <https://qiskit.org/>.

[35] A. Kandala, A. Mezzacapo, K. Temme, M. Takita, M. Brink, J. M. Chow, and J. M. Gambetta, Hardware-efficient variational quantum eigensolver for small molecules and quantum magnets, *Nature* **549**, 242 (2017).

[36] P. D. Nation, H. Kang, N. Sundaresan, and J. M. Gambetta, Scalable mitigation of measurement errors on quantum computers, *PRX Quantum* **2**, 040326 (2021).

[37] Error values from IBMQ Ehning on the 07.06.2023. Mean values for the chosen 4 qubits: $T_1 = 165\mu s$, $T_2 = 109\mu s$, readout error 1%, single-qubit gate-error 0.03%, CNOT-error 1.1%.

[38] O. Higgott, D. Wang, and S. Brierley, Variational quantum computation of excited states, *Quantum* **3**, 1 (2019).

[39] K. M. Nakanishi, K. Mitarai, and K. Fujii, Subspace-search variational quantum eigensolver for excited states, *Phys. Rev. Res.* **1**, 33062 (2019).

[40] J. R. McClean, M. E. Kimchi-Schwartz, J. Carter, and W. A. de Jong, Hybrid quantum-classical hierarchy for mitigation of decoherence and determination of excited states, *Phys. Rev. A* **95**, 042308 (2017).

[41] P. J. Ollitrault, A. Kandala, C.-F. Chen, P. K. Barkoutsos, A. Mezzacapo, M. Pistoia, S. Sheldon, S. Woerner, J. M. Gambetta, and I. Tavernelli, Quantum equation of motion for computing molecular excitation energies on a noisy quantum processor, *Phys. Rev. Res.* **2**, 043140 (2020).